Tailoring Spectrally Flat Infrared Photodetection with Thickness-Controlled Nanocrystalline Graphite

Naga Anirudh Peyyety, Sandeep Kumar, Min-Ken Li, Simone Dehm, and Ralph Krupke*

ABSTRACT: Graphene, a zero gap semiconductor, absorbs 2.3% of incident photons in a wide wavelength range as a free standing monolayer, whereas 50% is expected for ∼90 layers. Adjusting the layer number allows the tailoring of the photoresponse; however, controlling the thickness of multilayer graphene remains challenging on the wafer scale. Nanocrystalline graphene or graphite (NCG) can instead be grown with controlled thickness. We have fabricated photodetectors from NCG that are spectrally flat in the near infrared to short wavelength infrared region by tailoring the layer thicknesses. Transfer matrix simulations were used to determine the NCG thickness for maximum light absorption in the NCG layer on a silicon substrate. The extrinsic and intrinsic photoresponse was determined from 1100 to 2100 nm using chromatic aberration corrected photocurrent spectroscopy. Diffraction limited hyperspectral photocurrent imaging shows that the biased photoresponse is unipolar and homogeneous across the device area, whereas the short circuit photoresponse gives rise to positive and negative photocurrents at the electrodes. The intrinsic photoresponses are wavelength independent, indicative of bolometric and electrothermal photodetection.

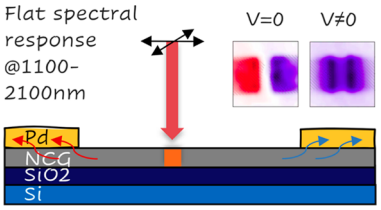

KEYWORDS: *photocurrent spectroscopy, imaging, near infrared, NIR, SWIR, nanocrystalline graphene, pyrolytic graphite, transfer matrix method*

INTRODUCTION

Photodetection in the near infrared (NIR) to short wavelength infrared (SWIR) electromagnetic spectrum has become very important for a wide range of applications in telecommunications, biomedical imaging, food inspection, night vision, environmental monitoring, and astronomy. Photodetectors used in this spectral range are commonly based on semiconductors such as HgCdTe, InGaAs, and Si,[1] where the material's band gap defines the spectral sensitivity. The more recently developed photosensitive semiconducting materials,[2] such as metal dichalcogenides,[3−6] titanium oxide−organic layers,[7] black phosphorous,[8] or perovskites,[9,10] have a similar operating principle. On the other hand, graphene is a photosensitive semimetal and an ideal wavelength independent photoabsorber for the visible to infrared wavelength range due to its linear band structure and the absence of a gap.[11] It is commercially available and CMOS compatible, and wired into a transistor configuration, graphene gives rise to photovoltaic, electrothermal, or bolometric photocurrents, depending on the operating conditions.[12−14] The bolometric photoresponse under a voltage bias has the advantage that the entire graphene channel becomes photosensitive, and responsivities comparable to that of p−n junctions have been demonstrated with visible light (2.5×10^{-4} A/W at 1 V bias and 690 nm).[14]

Photodetection with single layer graphene is limited by the low intrinsic light absorption of 2.3% and can only be enhanced by integrating graphene into optical cavities and plasmonic or photonic structures[15−18] or combining with quantum dots[19−23] or layered materials from the transition metal dichalcogenide family.[24,25] However, using optically engineered structures and materials with wavelength dependent light absorption inevitably induces a wavelength dependence in the responsivity,[17,26,27] which is not an obstacle unless spectral flatness is beneficial. In principle, the intrinsically flat optical broadband absorption of graphene could be improved simply by using several layers, and recently, the optical absorption was calculated for multilayer graphene taking into account the reflectance of each layer.[28] Interestingly, an almost wavelength independent light absorption of 50% was projected for graphite with 87 graphene layers, which promises an improvement in responsivity by an order of magnitude when used as a photodetector material. Unfortunately, it remains challenging to grow multilayer graphene with a predefined thickness. On the other hand, nanocrystalline graphene or graphite (NCG) can be grown directly on dielectric surfaces with a controllable thickness by graphitization of polymeric films[29−31] and have been employed as transparent electrodes for graphene glass and silicon based Schottky photodetectors.[32,33] Therefore, increasing the responsivity while keeping a

spectrally flat responsivity seems possible with thickness tailored NCG. We have previously demonstrated bolometric NIR photodetection with a 4 nm thin NCG layer.[31] However, due to the nonoptimized layer structure, the responsivity of the thin NCG layer was merely 1.7×10^{-6} A/W at 1 V bias and 1065 nm.

Here, in this work, we obtained spectrally flat infrared photoresponse with NCG on a SiO_2/Si substrate by tailoring the thickness of NCG and SiO_2. In the targeted NIR to SWIR, the responsivity exceeded the previous thin layer result by more than 2 orders of magnitude. The optimum SiO_2 and NCG thickness that is required for maximizing the optical absorption in NCG between 1100 and 2100 nm wavelengths was computed through transfer matrix simulations. Devices with source and drain electrodes were fabricated on the optimized NCG/SiO_2/Si layer structure. Scanning photo current measurements were conducted with an intensity calibrated, chromatic aberration corrected setup under short circuit and voltage bias conditions using a lock in technique to spectrally and spatially resolve photocurrents. The extrinsic and intrinsic responsivities were determined and analyzed in terms of the photodetection mechanism.

RESULTS AND DISCUSSION

Nanocrystalline graphite was grown on 300 nm SiO_2/Si substrates through the graphitization of a spin casted photo resist.[31] The photoresist solutions were prepared by diluting an S1805 photoresist in propylene glycol monomethyl ether acetate (PGMEA). NCG layers with 11 and 24 nm thicknesses were synthesized by adjusting the S1805/PGMEA dilution ratio and the spin casting conditions (Experimental Section).[31] After graphitization at 1000 °C for 10 h under high vacuum, the NCG thickness was measured using atomic force microscopy (AFM) (Figure S1) and characterized using Raman spectroscopy and optical imaging (Figure 1a,b). The Raman spectra of the NCG films show broad D , G , and 2D mode peaks, characteristic of nanocrystalline graphite.

The Raman spectra of the NCG films were analyzed to confirm the degree of sp^2 hybridization and to determine the average crystallite size, similar to our previous work where we determined the optimum graphitization conditions from Raman spectroscopy and X ray photoelectron spectroscopy.[31] The G peak position and the ratio of the D mode and G mode intensities have been fitted to the hybridization trajectory of Robertson and Ferrari,[34] showing that the NCG films are completely graphitized (100% sp^2 hybridization), as ex pected.[31] The crystallite size in the NCG films was determined from the width of the D peak to be 2−3 nm, which is similar to that obtained from our previous Raman and electron diffraction analyses.[31,35,36] Since the thickness of the synthesized graphitic films is larger than the crystallite size, we refer to the films in this work as nanocrystalline graphite. The thickness variation of the NCG films shown in Figure S13 is within 5% across the sample, and a corresponding statistical evaluation of the crystallite size is given in Figure S14. We note that the intensity of the Raman peaks is lower for the thicker film because of optical interference in the multilayer structure and reabsorption of the scattered light emanating from the lower part of the NCG layer by the upper part of the NCG layer. The Raman intensity of multilayer graphene on SiO_2/Si is not only dependent on the thickness of the graphitic layer and the oxide layer but also on the laser excitation wavelength and on the numerical aperture of the objective.[37]

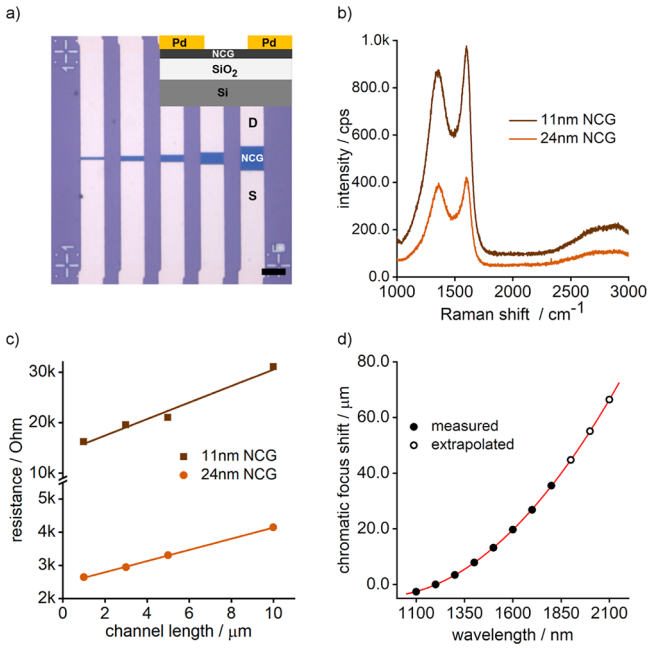

Figure 1. Fabrication and characterization of NCG devices. (a) Optical micrograph of NCG devices on 300 nm SiO_2/Si substrates with different channel lengths. Scale bar equals 10 μm. Inset shows a cross sectional view with the Pd source (S) and drain (D) electrodes. (b) Raman spectra of NCG/300 nm SiO_2/Si with 11 and 24 nm NCG thicknesses. (c) Device resistance vs channel length for the two NCG film thicknesses. (d) Axial chromatic focus shift of the 100× NIR objective.

NCG was finally patterned into the multi device layout shown in Figure 1a. The devices were fabricated by etching NCG into 100 μm long and 10 μm wide strips and depositing Pd/Cr source and drain contacts to form NCG channels of 10 μm width w and 1−10 μm lengths l (details given in the Experimental Section). The device resistance was determined from the linear current−voltage curves measured for each channel length. The intention of the large contact area between NCG and the metal electrodes was to minimize the contact resistance. Still, a contact resistance R_C is observed, which is not dependent on the channel length and shows up as an offset of the resistance versus channel length data, as shown in Figure 1c. R_C is very different for the two film thicknesses (14.2 kΩ@ 11 nm and 2.45 kΩ@24 nm), showing that the major contribution to R_C comes from the resistance of the NCG layer underneath the metal electrodes. The NCG sheet resistance R_S and the resistivity ρ were determined from the slope of the linear fit to the resistance versus channel length data. We obtain R_S = 16.4 kΩ and $\rho = 1.6 \times 10^{-4}$ Ωm for the 11 nm thick film and R_S = 1.6 kΩ and $\rho = 3.6 \times 10^{-5}$ Ωm for the 24 nm thick film. The resistivity values are comparable to those of thinner films prepared under identical graphitization con ditions with similar grain sizes ($\rho = 6 \times 10^{-5}$ Ωm@1 nm and 1.2×10^{-4} Ωm@6 nm).[31] The resistivity, however, is significantly different for the 11 and 24 nm thick NCG films. To explain why R_S changes by a factor of 10 although the thickness d of the 11 and 24 nm films differs by only a factor of 2.2, we must conclude that ρ is layer dependent ($R_S = \rho/d$). To trace the change in ρ to the microstructure is difficult. On one hand, the Raman D mode linewidth and the G mode position do not show any dependence on the layer thickness, which indicates that the average grain size is not thickness

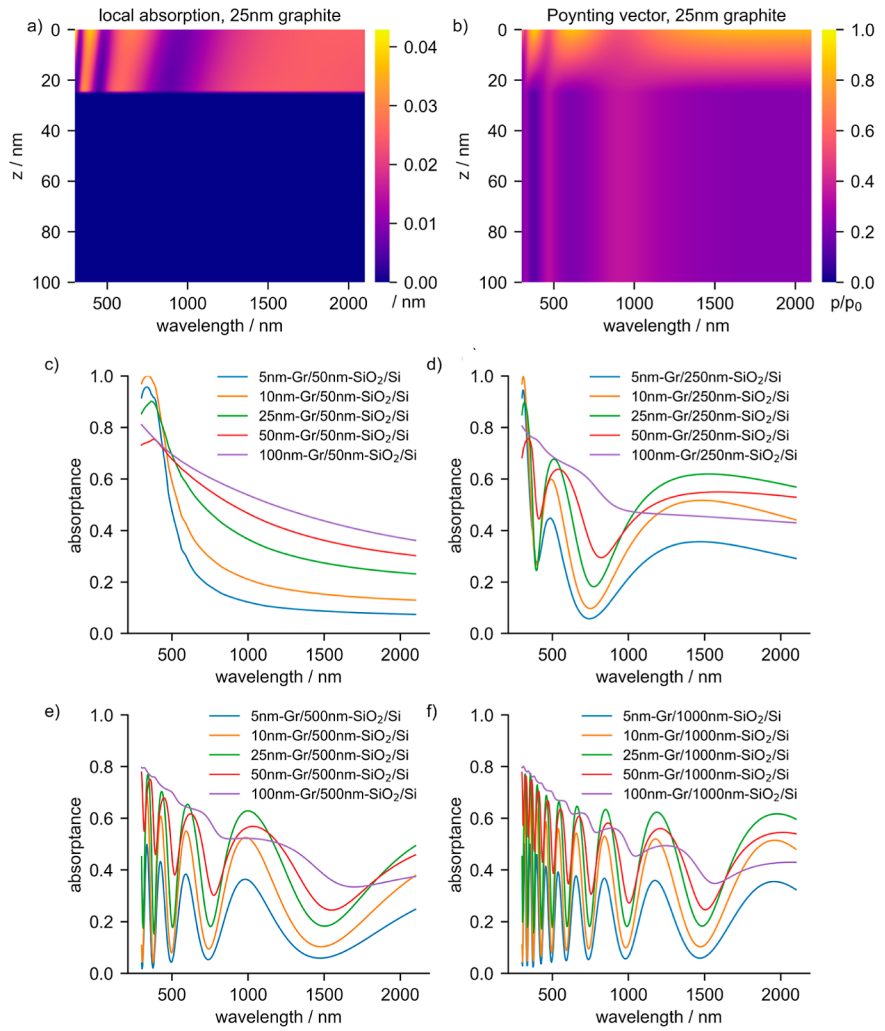

Figure 2. Transfer matrix simulation of (a) local absorption and (b) Poynting vector in a 25 nm graphite/300 nm SiO_2/Si multilayer. The z axis points along the surface normal into the substrate; the origin is at the graphite−air interface. (c−f) Calculated total absorptance in the graphite layer for different graphite and SiO_2 layer thicknesses, simulated with s polarized light under normal incidence.

dependent and neither is the degree of graphitization. On the other hand, the temperature dependence of the resistance presented in Figure S5 can be fitted to a variable range hopping mechanism, which is typical for polycrystalline graphitic films[38] and shows that grain boundaries are the limiting factor for the charge transport also in NCG. A small change in the tunneling barrier between the grains can lead to a change in the resistivity without leaving a trace in the structural analysis methods.

The optimum thickness of the NCG and SiO_2 layers on Si was determined using transfer matrix method (TMM) simulations to maximize the NIR to SWIR light absorption through the NCG layer. The calculations were performed with s polarized light under normal incidence in the 400−2100 nm wavelength range. The NCG and SiO_2 layer thicknesses were varied from 5 to 100 and 50 to 1000 nm, respectively, and the refractive index of the NCG layer was approximated using the wavelength dependent refractive index of graphite[28] (for TMM details, see the Experimental Section). Figure 2a,b shows the local light absorption and the Poynting vector—the directional energy flux—in the upper 100 nm region of a 25 nm graphite/300 nm SiO_2/Si layer structure. The results for the other layer thicknesses and probing depth are shown in Figures S2 and S3.

As expected, the local light absorption in the graphite layer is strongly dependent on wavelength and depth and, in turn, depends on the thickness of the graphite and SiO_2 layers. Relevant for photodetection is the integrated local light absorption in the graphite layer, the absorptance, which is shown for a wide range of parameters in Figure 2c−f. For a given oxide thickness, the fraction of light absorbed in graphite first increases with its thickness and then decreases as the reflectance from the graphite layer increases. In addition, the multilayer interference induces wavelength oscillations, which become more prominent for oxide layers thicker than 250 nm. As a result, for the targeted broad wavelength range from 1100 to 2100 nm, we found that the absorptance in graphite is maximized for 25 nm thick graphite on the top of a Si substrate with a 250 nm thick SiO_2 layer (green curve in Figure 2d). We used 300 nm thick SiO_2 instead because of commercial availability and the almost identical simulation results (Figure S4). We note that the optimized graphite thickness of 25 nm is close to the thickness that corresponds to the universal layer number $N = (2/\pi\alpha) = 87$ in graphite at an interlayer distance $d = 0.335$ nm. For values larger than $N \times d \approx 29$ nm, the reflectance of graphite becomes significant and its absorptance wavelength dependent.[28]

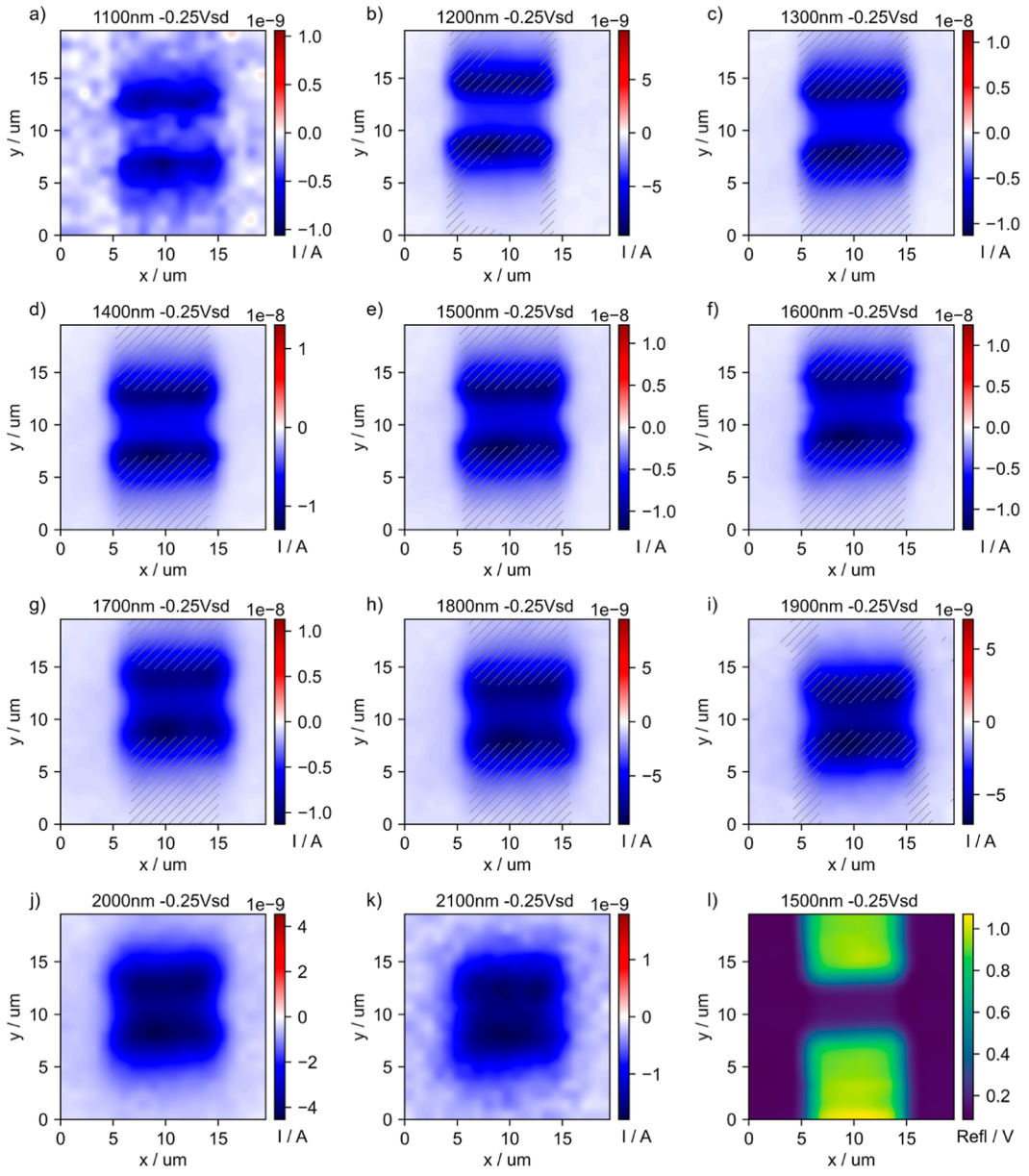

Figure 3. Scanning photocurrent imaging at −0.25 V source−drain bias. (a−k) Measurements obtained between 1100 and 2100 nm wavelengths using a device with 24 nm NCG layer thickness and 5 μm channel length. (l) Scanning reflectance images were recorded simultaneously, here shown at 1500 nm during the photocurrent scan. The reflectance data were superimposed on the photocurrent maps in (a−k) as gray shaded areas to indicate the position of the electrodes.

In the following, we describe the scanning photocurrent measurements. The devices were wire bonded to a chip carrier and mounted on a computer controlled photocurrent spec troscopy and imaging setup, consisting of an upright light microscope, motorized stages, a supercontinuum (SC) laser source, a lock in amplifier, a 2D SWIR camera, and a NIR photoreceiver. The broadband SC spectrum was transformed into a smooth power spectrum from 1100 to 2100 nm by implementing a wavelength−specific intensity adjustment to the acousto optic tunable filter (AOTF). The resulting power spectrum was gauged at the microscope objective output using a calibrated pyroelectric radiometer. Although an NIR objective is used, the setup exhibits significant chromatic aberration, resulting in an axial focus shift of 60 μm over the entire wavelength range, as shown in the wavelength dependent axial focus shift in Figure 1. Thus, the focus had to be adjusted for each wavelength to ensure diffraction limited photocurrent imaging at every wavelength. To image the laser spot, we used a 2D SWIR camera which is sensitive up to 1800 nm. Beyond 1800 nm, the chromatic focus shift was obtained by extrapolation. The chromatic aberration correction made it necessary to perform the hyperspectral photocurrent imaging by sequentially scanning an area for each wavelength instead of scanning the wavelength at each position. The photocurrents were measured using a lock in technique to probe the amplitude and the phase. The intensity modulation required for this was induced by the AOTF. Simultaneously with the photocurrent imaging, the laser signal reflected from the sample surface was recorded using a photoreceiver to image the electrodes and to correlate the photocurrent signal with the position of the laser spot. We note that thermal drifts were minimized through a concentric design of the setup. For

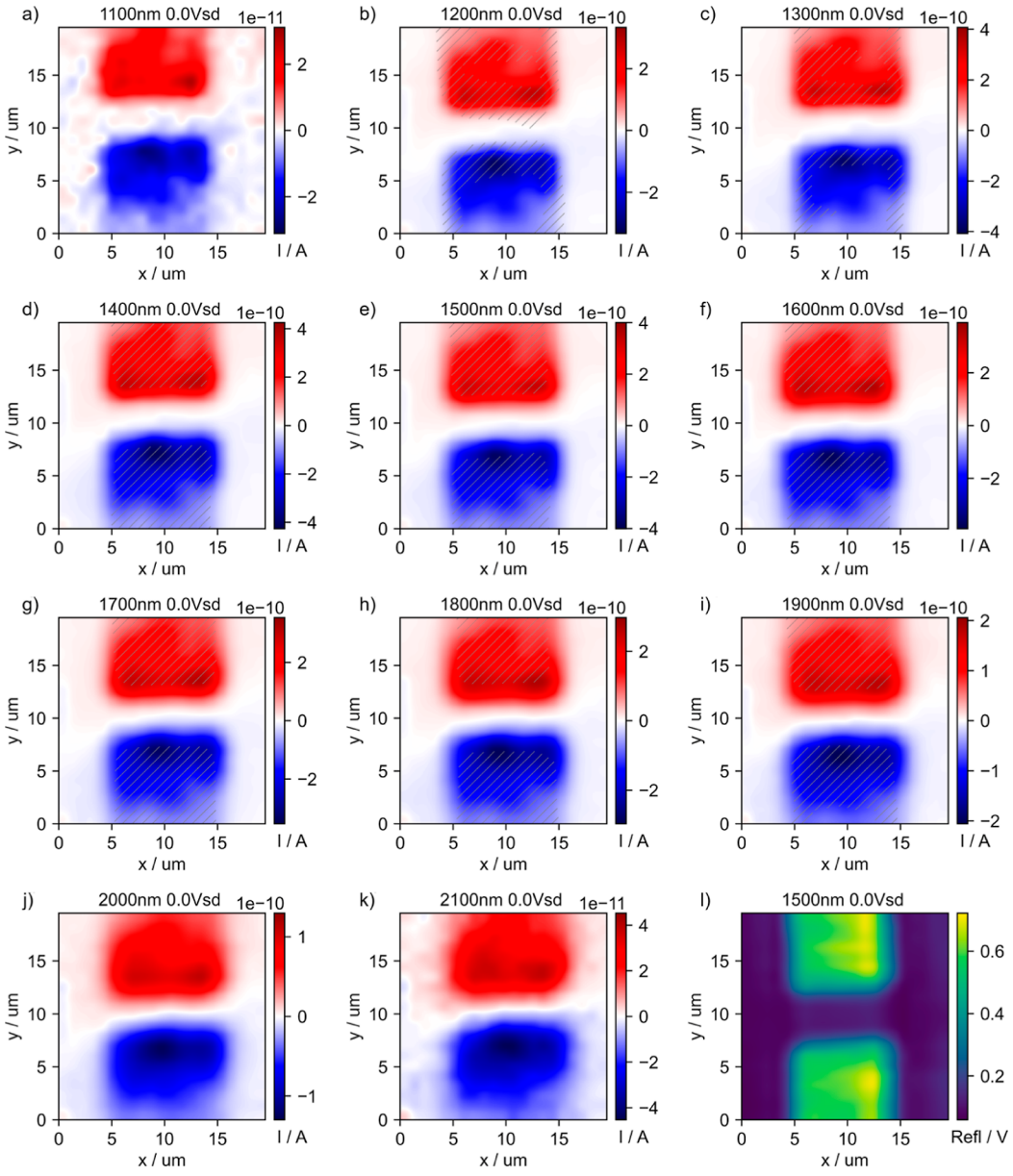

Figure 4. Scanning photocurrent imaging under short circuit conditions. (a–k) Measurements obtained between 1100 and 2100 nm wavelengths using a device with 24 nm NCG layer thickness and 5 μm channel length. (l) Scanning reflectance images were recorded simultaneously, here shown at 1500 nm during the photocurrent scan. The reflectance data were superimposed onto the photocurrent maps in (a–k) as gray shaded areas to indicate the position of the electrodes.

further details on the setup and procedures, see the Experimental Section and Supporting Information.

Figure 3a–k shows scanning photocurrent images of a device with 24 nm thick NCG and a channel length of 5 μm, recorded at 250 mV source–drain bias. The scans were acquired over a 20 μm × 20 μm area with 1 μm step size and a 1100–2100 nm wavelength range with 100 nm increments. The positions of the electrodes were determined for each scan from the reflectance measurement and overlayed as gray shaded areas to the corresponding photocurrent images. An exemplary reflectance image, recorded at 1500 nm, is given in Figure 3l. The photocurrents are plotted as the real part $I_{RE} = M \times \cos(\phi - \phi_{ref})$ from the magnitude M and the phase ϕ of the photocurrent signal, with the lock in reference oscillator phase ϕ_{ref} set to zero. We observe that photocurrents are generated in the entire NCG channel and the contact region and that the sign of the real photocurrent depends on the polarity of the applied external bias. An imaginary component was not detected. In our wiring scheme, the bias is applied to the drain and the photocurrent is measured at the source.[39] Identical signs of the photocurrent and the voltage bias mean in this experiment that the current increases when the light is on. Note that the dark current I_{dark} = 250 mV/3.3 kΩ = 75 μA is not detected via the lock in technique. For a voltage biased device, the photo induced increase of the current is due to a reduction of the resistance. Since NCG has no band gap, the illumination modulates the charge carrier transport rather than the charge carrier concentration. The relative change in resistance under illumination can be calculated from the photocurrent integrated over the device area $I_{INT\text{-}PC}$ and from the dark current I_{dark} as $(R_{illum} - R_{dark})/R_{dark} = (I_{INT\text{-}PC} + I_{dark} - I_{dark})/I_{dark}$, which yields ≈2% at 1500 nm with $I_{INT\text{-}PC} \approx 1.5$

μA. Since the absorbed photons are converted into heat, we have also measured the temperature dependence of the resistance of a thin NCG film (Figure S5). As expected for NCG, the resistance decreases with temperature due to thermally activated grain to grain tunneling of carriers, leading to variable range hopping in the nanocrystalline material.[40] At room temperature, we find the linear temperature coefficient of the resistivity $\alpha = \rho^{-1} \times d\rho/dT = -0.004\ K^{-1}$, which means that light induced heating by several kelvin leads to the measured photocurrents. Hence, we conclude that the photocurrent measured at a finite bias is bolometric.

It is instructive to look closer at the bolometric photocurrent distribution, which is determined from the local bolometric current density

$$\vec{j}_{bol} = -\alpha \times \rho^{-1} \times \Delta T \times \vec{E} \quad (1)$$

and depends not only on the temperature coefficient α, the resistivity ρ, and the photo induced change in temperature ΔT but also on the electric field E. The bolometric current is thus proportional to the electric field distribution and disappears in field free regions. From TMM simulations, we have determined that 14−20% of the light is absorbed by the Pd metal electrodes (Figure S6). The rest of the light is back reflected, and none is absorbed by the NCG underneath the Pd. As a result, the heating of NCG is much smaller underneath the Pd electrodes than that in the channel, where 60% of the light is absorbed by NCG. Still, the bolometric current close to the electrodes is larger than that in the center of the channel, which shows that the electric field is larger at the contact than that in the channel. This is not surprising since the resistance of the 5 μm long channel is 0.85 kΩ, whereas the resistance R_C of the regions next to the channel accounts for 2.45 kΩ. Hence, 74% of the applied bias drops off at the two contact regions. The bolometric current distribution shows that these regions are narrow and lead to a large electric field that is concentrated to a narrow region at the Pd electrodes. Since R_C is determined by the NCG thickness and not by the interface between NCG and Pd, the electric field distribution is very similar for the 11 nm NCG device, where we find that 71% of the applied bias drops at the contact region. Therefore, the photocurrent distribution looks similar for the thinner NCG film, as shown in Figure S7. We note that the temperature coefficient α of NCG is 1 order of magnitude larger than that of graphite,[41] resulting in a correspondingly higher bolometric responsivity (eq 1).

At zero bias, the scanning photocurrent images look very different, as shown in Figure 4a−k, for the same 24 nm thick NCG device. The data for the 11 nm thick layer are shown in Figure S8. Photocurrents are generated at the electrodes and with opposite signs at the source and drain electrodes. Furthermore, in the channel between the electrodes, the photocurrent is zero. Unlike in the bolometric case with an external bias voltage, the appearance of photocurrents at zero bias requires the generation of a photovoltage. The data show that this occurs over a large area of the electrodes where Pd forms an interface with NCG. As described before, light is not transmitted through the Pd layer and to a large extent is back reflected. However, 14−20% is absorbed in Pd and is thus indirectly heating the interface. This leads to the build up of a voltage across the interface as a result of the difference in the material Seebeck coefficients S_{NCG} and S_{Pd}. Such a photo thermoelectric (PTE) effect, induced by contact heating, has been observed previously on graphene/Au contacts.[42] The spatial extent of such a PTE photocurrent is determined by the heat diffusion and cooling in the structure and the distance of the laser spot from the electrode gap. As a result, the PTE photocurrent extends more into the electrodes than the bolometric photocurrent, which is limited to areas with electric fields induced by the external bias voltage. The PTE photovoltage V_{PTE} is determined by $V_{PTE} = (S_{Pd} - S_{NCG}) \times \Delta T$ and can be calculated from the PTE photocurrent, integrated over one electrode and multiplied with the device resistance. We find that V_{PTE} is on the order of 10 μV, which is reasonable assuming that ΔT is on the order of kelvin and $S_{Pd} - S_{NCG}$ on the order of microvolts per kelvin.[43,44] The enhanced PTE photocurrents at the corners of the electrodes is a typical signature of a local light field enhancement leading to enhanced light absorption and heating of the interface.[42]

For applications, the bolometric operation mode is advanta geous since the entire NCG channel is photoactive and the weak PTE photocurrents with opposing signs do not play a role if the applied voltage bias is larger than V_{PTE}. To quantify the targeted broadband response, we have determined the wavelength dependence of the device responsivity, the external responsivity. We first integrated the scanning photocurrent maps over the device area for each wavelength to obtain the photocurrent spectrum shown in Figure 5a. The parabola

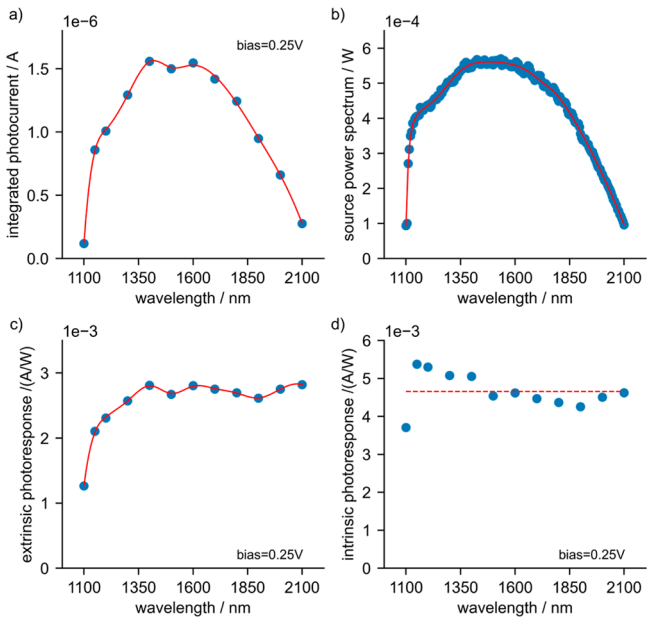

Figure 5. Spectroscopic analysis. (a) Integrated photocurrent obtained from the scanning photocurrent maps in Figure 3 of the 24 nm thick NCG device. (b) Calibrated power spectrum measured after the wavelength specific intensity adjustment of the SC light source by the AOTF. (c) Extrinsic photoresponse from the normalization of the integrated photocurrent with the power spectrum. (d) Intrinsic photoresponse from the normalization of the extrinsic photoresponse with the graphite absorptance.

shaped wavelength dependence originates from the spectrum of the light source (Figure 5b), and the external photoresponse was then calculated by normalizing the photocurrent spectrum with the source spectrum. Figure 5c shows that the device responsivity is about 2.8×10^{-3} A/W over a wide wavelength range. The responsivity falls off below 1300 nm due to the weaker absorptance of light in the NCG layer for the selected

layer thicknesses of NCG and SiO_2 on Si (green curve in Figure S4). If we normalize the extrinsic responsivity with the simulated NCG light absorptance, we obtain a nearly flat intrinsic responsivity within a 15% range around 4.7×10^{-3} A/W (Figure 5d). The specific detectivity D^* for the 24 nm thick NCG device is 10^6 jones at 0.25 V bias and 1500 nm. We have used the expression $D^* = R \times (A/(2 \times q \times I_{dark}))^{0.5}$ with I_{dark} = 75 μA, device area $A = (5 \times 10)$ μm^2, the responsivity R, and the elementary charge q because our device is shot noise limited.[45] The spectroscopic analysis for the 11 nm thick NCG device is given in Figure S9a–d. The weak wavelength dependence is a consequence of the approximation of the optical properties of NCG by graphite in the TMM simulations, which is good but not perfect. This conclusion can be drawn because the responsivity over wavelength is plotted in units of current per power. A bolometric photocurrent is proportional to the absorbed power and hence is wavelength independent for constant absorbed power. The same would be true for a PTE photocurrent. In contrast, a photovoltaic current would be proportional to the photon flux not the power. Concerning other thin film/2D photodetectors, the bolometric responsivity of NCG is quite comparable, with the benefit that the NCG devices require a rather low bias voltage (see the table in the Supporting Information). Also, the spectral flatness, that can be shifted to other wavelength ranges, in combination with the absence of an intrinsic wavelength cutoff in the absorption makes NCG a potentially interesting material for longer wavelength detection. Furthermore, the NCG photodetectors are made of nontoxic materials and are RoHS compliant. Unfortunately, the detectivity is rather low and in the same range as that of carbon nanotube based broadband photodetectors[46] but nevertheless sufficient for spectroscopy and imaging with moderate light power sources. An improvement toward sensing lower light levels could be realized by using a higher bias and a modified structure. For instance, the addition of a reflective layer underneath the thickness optimized NCG layer would result in a near unity absorptance and enhance the responsivity while preserving the spectral flatness. Also, the thermalization by the substrate could be eliminated by underetching the NCG layer to reach a higher ΔT. We also envision an optimization of the device geometry to maximize the electric field within the channel region and hence the bolometric response.

The use of the locally integrated photocurrent to determine the photoresponse requires explanation. In our scanning photocurrent measurements, the photoactive device area is larger than the laser spot size. As a result, the measured photocurrent under local illumination is not equivalent to measurements under global illumination. This can be understood when treating the channel as a 2D network of resistors.[47] Under local illumination, the resistance of the illuminated area changes, while the resistance in the nonilluminated area remains unchanged. As a result, the current distribution in the biased channel depends on the size and the position of the illuminated area. We simulated the scanning photocurrent experiment by solving the stationary continuity equation of the bolometric photocurrent $\nabla \vec{j}_{bol} = 0$ using a finite element method (FEM) solver in two dimensions. The illuminated spot within the simulated channel was mimicked as a region with reduced resistivity, and the current was calculated with Dirichlet and Neumann boundary conditions for the potential at the sides with and without electric contacts, respectively (details in the Experimental Section). The scanning photo current measurement was simulated by calculating the current for every position of the laser spot, keeping the step size of the raster scan equal to the spot size. The simulation shows that spatially integrating the scanning photocurrent is equivalent to measurements under global illumination with the same light intensity per area, provided that r, the ratio between the resistivity with and without illumination, approaches unity, as shown in Figure S10. In our experiment, r is only a few percent, and the method is therefore applicable. A final comment on the thickness dependence of the photoresponse of the NCG films should be mentioned. Figure S11a–c shows the local absorption, the Poynting vector, and the resulting absorptance in the graphite layer versus the graphite layer thickness at 1550 nm wavelength. The simulations show that reducing the NCG thickness from 24 to 11 nm reduced the absorptance by 10%. However, the measured photoresponse of the 11 nm NCG device is ~3 times lower than that of the device with the optimum NCG thickness of 24 nm (Figure S11d). This is understood by the ~4 times higher resistivity of the thinner NCG layer, likely due to a thickness dependent grain structure of the NCG film, which leads to a larger reduction in the photoresponse for the thinner film, as expected solely from light absorptance.

CONCLUSIONS

In summary, spectrally flat broadband photodetection in the NIR to SWIR region has been realized using light field simulation optimized nanocrystalline graphite on SiO_2/Si substrates. The flat responsivity is not limited to the chosen wavelength range and can be adjusted to other parts in the electromagnetic spectrum by tailoring the layer thickness of NCG and SiO_2 accordingly. This optimization is possible because the absorptance of graphite is wavelength independent up to 30 nm thickness. This conceptually new approach could be of interest when spectral flatness over an extended wavelength range is important. Compared to that of previous studies with thinner films, the bolometric photoresponse at moderate voltage bias is 2 orders of magnitude larger and has the potential to be further improved through grain size and grain boundary engineering,[48,49] back reflective coating, thermal decoupling, and electric field optimization.

EXPERIMENTAL SECTION

NCG Synthesis and Device Fabrication. Thermally grown 300 nm SiO_2 on p Si (boron doping, ρ < 0.005 Ωcm, Active Business Company) wafers were cut into 10 mm × 10 mm size, sonicated in acetone, rinsed with isopropanol, and exposed to a mild oxygen plasma. A pre baking step at 110 °C on a hot plate for 120 s removed the physisorbed water. NCG films were grown on the soft baked SiO_2/Si substrates using the S1805 photoresist (MICROPOSIT) as a carbon source. The photoresist was diluted to a 1:4 and 1:1 ratio using PGMEA, and 35 μL of the prepared resist solution was spin coated at 3000 and 4000 rpm for 30 s to target final NCG thicknesses of 10 and 24 nm, respectively. The spin coated substrates were baked at 110 °C for 60 s on a hot plate to allow outgassing of the solvent. After the post baking step, the substrates were loaded into the vacuum furnace for graphitization of the photoresist film at 1000 °C at 10^{-6} mbar pressure. The thickness of the synthesized NCG film was measured using the atomic force microscope (Bruker Dimension Icon) in the tapping mode. The NCG films were characterized using Raman spectroscopy (Renishaw inVia Microscope) at 532 nm laser excitation, 3 mW power, 10 s integration time, and 20× (NA = 0.4) magnification. The device fabrication on the substrates with the NCG film was realized in three steps. In the first step, tungsten alignment markers were defined by standard electron beam lithography (Leo

1530 with Raith ELPHY Plus pattern generator) and sputter deposition. In the second step, areas of interest of the NCG film were patterned using the position of tungsten alignment markers defined in the first step. For patterning the NCG film, poly(methyl methacrylate) (PMMA 950 k, 8% in anisol) was spin coated at 6000 rpm to result in a 700 nm thick layer, which also acted as an etch mask. The exposed PMMA after electron beam patterning was developed in a solution of methyl isobutyl ketone (MIBK) and isopropanol (1:3 ratio) for 30 s at room temperature and baked on a hot plate for 60 s at 90 °C. The patterned NCG film unprotected by PMMA was etched using an O_2 plasma in a reactive ion etching system (Oxford Plasmalab 80 Plus) at 15 sccm O_2, 30 W, and 60 mTorr for 4 min and 15 s. The remaining protective PMMA layer after the etching step was removed using acetone. In the final lithography step, the electrode area was defined using electron beam patterning with conditions identical to those in the first and second lithography steps. The 45 nm thick Pd/Cr metal was then sputtered as an electrode material for source and drain contacts. The fabricated devices were vacuum annealed at 430 °C for 60 min to remove PMMA residues. The devices were then wire bonded onto a ceramic chip carrier for the photocurrent measurements. We have fabricated in total 16 devices, eight for each of the two layer thicknesses. From the statistical evaluation, we have determined that the standard deviations of the film thicknesses and the sheet resistances are below 10%, which is similar to the device to device deviation that we observe in photocurrent and responsivity.

Photocurrent Measurements. The photocurrent maps were recorded in the NIR/SWIR spectral range from 1100 to 2100 nm using a SC white light source (SuperK Extreme EXW 12, NKT Photonics). An AOTF (SuperK Select nIR2 AOTF attached to SuperK connector with FD6 PM fiber) converts the SC white light source into a tunable laser source. The excitation laser line from the AOTF was then coupled to a reflective collimator (Thorlabs RC02FC P01), and 90% of the collimated light is guided through the 90:10 beam splitter (Thorlabs BS030) into the customized Zeiss Axiotech VARIO microscope with an NIR objective. The laser source intensity was continuously monitored during the photocurrent scan using a NIR photodiode sensor (PD300R IR, Ophir) attached at the 10% exit port. The photocurrent maps were recorded in 100 nm wavelength steps. The diffraction limited laser spot was focused onto the sample using the infinity corrected 100× NIR (Mitutoyo M PLAN APO, 0.50 NA) long working distance objective, and the laser spot was positioned across the scan area (20 μm × 20 μm) with a stepper motor controlled $X-Y$ translation stage (8MTF 102LS05, Standa) in 1 μm steps. The laser spot reflected from the sample surface was imaged using a Peltier cooled InGaAs camera (WiDy Sens 640V ST, New Imaging Technologies). The fine adjustment of the focus was precisely controlled using a piezo objective scanner (PIFOC P 712.CDQ, Physik Instrumente). The chromatic aberration induced shift of the axial focus of the NIR objectives was compensated for each wavelength before obtaining a photocurrent map. A wavelength−specific intensity adjustment to the AOTF was implemented to obtain a smooth, intensity calibrated source spectrum (Figure S12). The photocurrent of the NCG films was measured using the lock in technique at room temperature. The incident light was modulated at 1214 Hz via the AOTF SuperK COMMAND interface box. The frequency was selected in a low noise region remote from multiple power line signals analyzed using a spectrum analyzer (Signal Hound USB SA44B) at the lock in monitor output. The modulated photocurrent was converted into a voltage signal using a low noise current preamplifier (DLPCA 200, Femto) and fed into the lock in amplifier (SR830 Lock in Amplifier, Stanford Research Systems) referenced to the modulation frequency. The photocurrent amplitude and phase were subsequently recovered from the lock in amplifier. For the biased photocurrent measurements, a source−drain bias was applied via the auxiliary output of the lock in amplifier. In sync with the photocurrent mapping, the back reflected light from the sample was simultaneously recorded to map out the device area using an InGaAs photoreceiver (OE 200 IN2, Femto) connected to the source meter (Keithley 6430). The photocurrent and reflectance mapping were automated and controlled using a python code. The current−voltage device characteristics in the dark were also measured in the photocurrent setup. A dc bias in steps of 50 mV from −0.25 to 0.25 V was applied to the drain electrode via the Aux out of the lock in amplifier with the source electrode connected to the current preamplifier. The dc voltage signal from the current preamplifier was read out via the Aux in of the lock in amplifier.

Simulations. TMM simulations were conducted for s polarized light at normal incidence using a python code available at github.com/krupke group based on the TMM code of Steve Byrnes (arXiv:1603.02720; github.com/sbyrnes321/tmm). The complex refractive index of NCG was approximated by the optical constants of graphite, calculated from an analytical expression based on the dynamical conductivity of graphite.[28] The optical constants for Si and SiO_2 were taken from the refractiveindex.info database (SiO_2: Lemarchand 2013, Si: Aspnes and Studna 1983), extended with NIR data for Si from the filmetrics.de database. FEM simulations of the bolometric photocurrent were performed using the commercial software package FlexPDE 6.5. A squared 2D simulation space was confined by two Dirichlet boundaries, defining the potential difference from the applied bias voltage, and by Neumann boundaries for the two noncontacted sides. Inside the boundaries, the material was defined by its resistivity in the dark ρ_{dark} and under illumination ρ_{light}. The scanning photocurrent measurement was mimicked by defining an illuminated square with ρ_{light}, surrounded by the remaining area with ρ_{dark}. The current was simulated for each position of the illumination square within the simulation space, and the bolometric current was determined by subtraction of the current without illumination. Simulations were performed for raster scans between 2 × 2 and 50 × 50 (yielding similar results) and for resistivity ratios ρ_{light}/ρ_{dark} between 0.001 and 0.99. The FlexPDE script for simulating the scanning photocurrent imaging and the python code for the analysis is available at github.com/krupke group.

■ ASSOCIATED CONTENT

AFM analysis; TMM simulations of local absorption and the Poynting vector; absorptance in the graphite layers on 300 nm SiO_2/Si; temperature dependence of NCG sheet resistance; TMM simulation of absorptance and reflectance of 45 nm Pd/graphite/SiO_2/Si; scanning photocurrent imaging under source−drain bias and short circuit condition for the 11 nm NCG devices; spectroscopic analysis of the 11 nm NCG device; simulation result from solving the continuity equation for the bolometric photocurrent; local absorption, Poynting vector, and absorptance at 1550 nm; thickness analysis of the NCG film; hybridization and crystallite size analysis of NCG films; description of the setup design; and compilation of photodetector key performance figures (PDF)

■ AUTHOR INFORMATION

Corresponding Author

Ralph Krupke − *Institute of Nanotechnology, Karlsruhe Institute of Technology, 76021 Karlsruhe, Germany; Institute of Quantum Materials and Technologies, Karlsruhe Institute of Technology, 76021 Karlsruhe, Germany; Institute of Materials Science, Technische Universität Darmstadt, 64287 Darmstadt, Germany;* orcid.org/0000 0001 8427 8592; Email: krupke@kit.edu

Authors

Naga Anirudh Peyyety − *Institute of Nanotechnology, Karlsruhe Institute of Technology, 76021 Karlsruhe, Germany; Institute of Materials Science, Technische Universität Darmstadt, 64287 Darmstadt, Germany;* orcid.org/0000 0002 4822 3575

Sandeep Kumar − *Institute of Nanotechnology, Karlsruhe Institute of Technology, 76021 Karlsruhe, Germany; Institute of Materials Science, Technische Universität Darmstadt, 64287 Darmstadt, Germany*

Min Ken Li − *Institute of Quantum Materials and Technologies, Karlsruhe Institute of Technology, 76021 Karlsruhe, Germany; Institute of Materials Science, Technische Universität Darmstadt, 64287 Darmstadt, Germany*

Simone Dehm − *Institute of Nanotechnology, Karlsruhe Institute of Technology, 76021 Karlsruhe, Germany*

Author Contributions

The experiments were conceived and designed by R.K. and N.A.P. Devices were fabricated and characterized by N.A.P. with inputs from S.D., S.K., M. K.L., and R.K. Simulations were performed by R.K. and N.A.P. The manuscript was written by N.A.P. and R.K., with inputs from all coauthors.

Notes

The authors declare no competing financial interest.

■ ACKNOWLEDGMENTS

N.A.P. received funding from the German Research Foundation (DFG) project KR 3670/6 1, and S.K. received funding from the German Research Foundation (DFG) project KR 3670/3 1. M. K.L., S.D., and R.K. received funding from the Helmholtz Research Programs Natural, Artificial and Cognitive Information Processing (NACIP) and Materials Systems Engineering (MSE), and support from the Karlsruhe Nano Micro Facility (KNMF).

■ REFERENCES

(1) Downs, C.; Vandervelde, T. Progress in Infrared Photodetectors Since 2000. *Sensors* **2013**, *13*, 5054−5098.

(2) Chen, H.; Liu, H.; Zhang, Z.; Hu, K.; Fang, X. Nanostructured Photodetectors: From Ultraviolet to Terahertz. *Adv. Mater.* **2016**, *28*, 403−433.

(3) Liang, Q.; Wang, Q.; Zhang, Q.; Wei, J.; Lim, S. X.; Zhu, R.; Hu, J.; Wei, W.; Lee, C.; Sow, C.; Zhang, W.; Wee, A. T. S. High Performance, Room Temperature, Ultra Broadband Photodetectors Based on Air Stable $PdSe_2$. *Adv. Mater.* **2019**, *31*, 1807609.

(4) Yim, C.; McEvoy, N.; Riazimehr, S.; Schneider, D. S.; Gity, F.; Monaghan, S.; Hurley, P. K.; Lemme, M. C.; Duesberg, G. S. Wide Spectral Photoresponse of Layered Platinum Diselenide Based Photodiodes. *Nano Lett.* **2018**, *18*, 1794−1800.

(5) Wang, Q.; Lai, J.; Sun, D. Review of Photo Response in Semiconductor Transition Metal Dichalcogenides Based Photo sensitive Devices. *Opt. Mater. Express* **2016**, *6*, 2313.

(6) Xie, Y.; Zhang, B.; Wang, S.; Wang, D.; Wang, A.; Wang, Z.; Yu, H.; Zhang, H.; Chen, Y.; Zhao, M.; Huang, B.; Mei, L.; Wang, J. Ultrabroadband MoS_2 Photodetector with Spectral Response from 445 to 2717nm. *Adv. Mater.* **2017**, *29*, 1605972.

(7) Yan, T.; Cai, S.; Hu, Z.; Li, Z.; Fang, X. Ultrafast Speed, Dark Current Suppression, and Self Powered Enhancement in TiO_2 Based Ultraviolet Photodetectors by Organic Layers and Ag Nanowires Regulation. *J. Phys. Chem. Lett.* **2021**, *12*, 9912−9918.

(8) Youngblood, N.; Chen, C.; Koester, S. J.; Li, M. Waveguide Integrated Black Phosphorus Photodetector with High Responsivity and Low Dark Current. *Nat. Photonics* **2015**, *9*, 247−252.

(9) Li, C.; Wang, H.; Wang, F.; Li, T.; Xu, M.; Wang, H.; Wang, Z.; Zhan, X.; Hu, W.; Shen, L. Ultrafast and Broadband Photodetectors Based on a Perovskite/Organic Bulk Heterojunction for Large Dynamic Range Imaging. *Light Sci. Appl.* **2020**, *9*, 31.

(10) Li, Z.; Liu, X.; Zuo, C.; Yang, W.; Fang, X. Supersaturation Controlled Growth of Monolithically Integrated Lead Free Halide Perovskite Single Crystalline Thin Film for High Sensitivity Photo detectors. *Adv. Mater.* **2021**, *33*, 2103010.

(11) Bonaccorso, F.; Sun, Z.; Hasan, T.; Ferrari, A. C. Graphene Photonics and Optoelectronics. *Nat. Photonics* **2010**, *4*, 611−622.

(12) Xia, F.; Mueller, T.; Golizadeh Mojarad, R.; Freitag, M.; Lin, Y. m.; Tsang, J.; Perebeinos, V.; Avouris, P. Photocurrent Imaging and Efficient Photon Detection in a Graphene Transistor. *Nano Lett.* **2009**, *9*, 1039−1044.

(13) Song, J. C. W.; Rudner, M. S.; Marcus, C. M.; Levitov, L. S. Hot Carrier Transport and Photocurrent Response in Graphene. *Nano Lett.* **2011**, *11*, 4688−4692.

(14) Freitag, M.; Low, T.; Xia, F.; Avouris, P. Photoconductivity of Biased Graphene. *Nat. Photonics* **2013**, *7*, 53−59.

(15) Echtermeyer, T. J.; Britnell, L.; Jasnos, P. K.; Lombardo, A.; Gorbachev, R. V.; Grigorenko, A. N.; Geim, A. K.; Ferrari, A. C.; Novoselov, K. S. Strong Plasmonic Enhancement of Photovoltage in Graphene. *Nat. Commun.* **2011**, *2*, 458.

(16) Gan, X.; Shiue, R. J.; Gao, Y.; Meric, I.; Heinz, T. F.; Shepard, K.; Hone, J.; Assefa, S.; Englund, D. Chip Integrated Ultrafast Graphene Photodetector with High Responsivity. *Nat. Photonics* **2013**, *7*, 883−887.

(17) Engel, M.; Steiner, M.; Lombardo, A.; Ferrari, A. C.; Löhneysen, H. V.; Avouris, P.; Krupke, R. Light−Matter Interaction in a Microcavity Controlled Graphene Transistor. *Nat. Commun.* **2012**, *3*, 906.

(18) Schuler, S.; Schall, D.; Neumaier, D.; Schwarz, B.; Watanabe, K.; Taniguchi, T.; Mueller, T. Graphene Photodetector Integrated on a Photonic Crystal Defect Waveguide. *ACS Photonics* **2018**, *5*, 4758−4763.

(19) Konstantatos, G.; Badioli, M.; Gaudreau, L.; Osmond, J.; Bernechea, M.; de Arquer, F. P. G.; Gatti, F.; Koppens, F. H. L. Hybrid Graphene−Quantum Dot Phototransistors with Ultrahigh Gain. *Nat. Nanotechnol.* **2012**, *7*, 363−368.

(20) Nikitskiy, I.; Goossens, S.; Kufer, D.; Lasanta, T.; Navickaite, G.; Koppens, F. H. L.; Konstantatos, G. Integrating an Electrically Active Colloidal Quantum Dot Photodiode with a Graphene Phototransistor. *Nat. Commun.* **2016**, *7*, 11954.

(21) Ni, Z.; Ma, L.; Du, S.; Xu, Y.; Yuan, M.; Fang, H.; Wang, Z.; Xu, M.; Li, D.; Yang, J.; Hu, W.; Pi, X.; Yang, D. Plasmonic Silicon Quantum Dots Enabled High Sensitivity Ultrabroadband Photo detection of Graphene Based Hybrid Phototransistors. *ACS Nano* **2017**, *11*, 9854−9862.

(22) Ahn, S.; Chung, H.; Chen, W.; Moreno Gonzalez, M. A.; Vazquez Mena, O. Optoelectronic Response of Hybrid PbS QD/Graphene Photodetectors. *J. Chem. Phys.* **2019**, *151*, 234705.

(23) Chiang, C. W.; Haider, G.; Tan, W. C.; Liou, Y. R.; Lai, Y. C.; Ravindranath, R.; Chang, H. T.; Chen, Y. F. Highly Stretchable and Sensitive Photodetectors Based on Hybrid Graphene and Graphene Quantum Dots. *ACS Appl. Mater. Interfaces* **2016**, *8*, 466−471.

(24) Roy, K.; Padmanabhan, M.; Goswami, S.; Sai, T. P.; Ramalingam, G.; Raghavan, S.; Ghosh, A. Graphene−MoS_2 Hybrid Structures for Multifunctional Photoresponsive Memory Devices. *Nat. Nanotechnol.* **2013**, *8*, 826−830.

(25) Koppens, F. H. L.; Mueller, T.; Avouris, P.; Ferrari, a. C.; Vitiello, M. S.; Polini, M. Photodetectors Based on Graphene, Other Two Dimensional Materials and Hybrid Systems. *Nat. Nanotechnol.* **2014**, *9*, 780−793.

(26) Furchi, M.; Urich, A.; Pospischil, A.; Lilley, G.; Unterrainer, K.; Detz, H.; Klang, P.; Andrews, A. M.; Schrenk, W.; Strasser, G.;

Mueller, T.; Mueller, T. Microcavity Integrated Graphene Photo detector. *Nano Lett.* **2012**, *12*, 2773−2777.
(27) Zhou, K.; Cheng, Q.; Song, J.; Lu, L.; Luo, Z. Highly Efficient Narrow Band Absorption of a Graphene Based Fabry−Perot Structure at Telecommunication Wavelengths. *Opt. Lett.* **2019**, *44*, 3430.
(28) Sasaki, K.; Hitachi, K. Universal Layer Number in Graphite. *Commun. Phys.* **2020**, *3*, 90.
(29) Zhang, Z.; Ge, B.; Guo, Y.; Tang, D.; Wang, X.; Wang, F. Catalyst Free Growth of Nanocrystalline Graphene/Graphite Patterns from Photoresist. *Chem. Commun.* **2013**, *49*, 2789.
(30) Son, S. Y.; Noh, Y. J.; Bok, C.; Lee, S.; Kim, B. G.; Na, S. I.; Joh, H. I. One Step Synthesis of Carbon Nanosheets Converted from a Polycyclic Compound and Their Direct Use as Transparent Electrodes of ITO Free Organic Solar Cells. *Nanoscale* **2014**, *6*, 678−682.
(31) Riaz, A.; Pyatkov, F.; Alam, A.; Dehm, S.; Felten, A.; Chakravadhanula, V. S. K.; Flavel, B. S.; Kübel, C.; Lemmer, U.; Krupke, R. Light Emission, Light Detection and Strain Sensing with Nanocrystalline Graphene. *Nanotechnology* **2015**, *26*, 325202.
(32) Zhang, Z.; Guo, Y.; Wang, X.; Li, D.; Wang, F.; Xie, S. Direct Growth of Nanocrystalline Graphene/Graphite Transparent Electro des on Si/SiO_2 for Metal Free Schottky Junction Photodetectors. *Adv. Funct. Mater.* **2014**, *24*, 835−840.
(33) Zhang, Q.; Tang, L.; Luo, J.; Zhang, J.; Wang, X.; Li, D.; Yao, Y.; Zhang, Z. Direct Growth of Nanocrystalline Graphene/Graphite All Carbon Transparent Electrode for Graphene Glass and Photo detectors. *Carbon* **2017**, *111*, 1−7.
(34) Ferrari, A. C.; Robertson, J. Resonant Raman Spectroscopy of Disordered, Amorphous, and Diamond like Carbon. *Phys. Rev. B: Condens. Matter Mater. Phys.* **2001**, *64*, 1−13.
(35) Shyam Kumar, C. N.; Chakravadhanula, V. S. K.; Riaz, A.; Dehm, S.; Wang, D.; Mu, X.; Flavel, B.; Krupke, R.; Kübel, C. Understanding the Graphitization and Growth of Free Standing Nanocrystalline Graphene Using in Situ Transmission Electron Microscopy. *Nanoscale* **2017**, *9*, 12835−12842.
(36) Kumar, C. N. S.; Konrad, M.; Chakravadhanula, V. S. K.; Dehm, S.; Wang, D.; Wenzel, W.; Krupke, R.; Kübel, C. Nano crystalline Graphene at High Temperatures: Insight into Nanoscale Processes. *Nanoscale Adv.* **2019**, *1*, 2485.
(37) Li, X. L.; Qiao, X. F.; Han, W. P.; Lu, Y.; Tan, Q. H.; Liu, X. L.; Tan, P. H. Layer Number Identification of Intrinsic and Defective Multilayered Graphenes up to 100 Layers by the Raman Mode Intensity from Substrates. *Nanoscale* **2015**, *7*, 8135−8141.
(38) Nakamura, S.; Miyafuji, D.; Fujii, T.; Matsui, T.; Fukuyama, H. Low Temperature Transport Properties of Pyrolytic Graphite Sheet. *Cryogenics* **2017**, *86*, 118−122.
(39) Riaz, A.; Alam, A.; Selvasundaram, P. B.; Dehm, S.; Hennrich, F.; Kappes, M. M.; Krupke, R. Near Infrared Photoresponse of Waveguide Integrated Carbon Nanotube−Silicon Junctions. *Adv. Electron. Mater.* **2019**, *5*, 1800265.
(40) Turchanin, A.; Weber, D.; Büenfeld, M.; Kisielowski, C.; Fistul, M. V.; Efetov, K. B.; Weimann, T.; Stosch, R.; Mayer, J.; Gölzhäuser, A. Conversion of Self Assembled Monolayers into Nanocrystalline Graphene: Structure and Electric Transport. *ACS Nano* **2011**, *5*, 3896−3904.
(41) Primak, W.; Fuchs, L. H. Electrical Conductivities of Natural Graphite Crystals. *Phys. Rev.* **1954**, *95*, 22−30.
(42) Tielrooij, K. J.; Massicotte, M.; Piatkowski, L.; Woessner, A.; Ma, Q.; Jarillo Herrero, P.; Hulst, N. F. v.; Koppens, F. H. L. Hot Carrier Photocurrent Effects at Graphene−Metal Interfaces. *J. Phys.: Condens. Matter* **2015**, *27*, 164207.
(43) Blackman, L. C. F.; Dundas, P. H.; Ubbelohde, A. R. J. P. The Anisotropic Thermoelectric Power of Graphite. *Proc. R. Soc. London, Ser. A* **1960**, *255*, 293−306.
(44) *CRC Handbook of Thermoelectrics*; Rowe, D. M., Ed.; CRC Press, 2018.
(45) Gong, X.; Tong, M.; Xia, Y.; Cai, W.; Moon, J. S.; Cao, Y.; Yu, G.; Shieh, C. L.; Nilsson, B.; Heeger, A. J. High Detectivity Polymer Photodetectors with Spectral Response from 300nm to 1450nm. *Science* **2009**, *325*, 1665−1667.
(46) St Antoine, B. C.; Ménard, D.; Martel, R. Single Walled Carbon Nanotube Thermopile For Broadband Light Detection. *Nano Lett.* **2011**, *11*, 609−613.
(47) Darwish, M.; Boysan, H.; Liewald, C.; Nickel, B.; Gagliardi, A. A Resistor Network Simulation Model for Laser Scanning Photo Current Microscopy to Quantify Low Conductance Regions in Organic Thin Films. *Org. Electron.* **2018**, *62*, 474−480.
(48) Zhao, T.; Xu, C.; Ma, W.; Liu, Z.; Zhou, T.; Liu, Z.; Feng, S.; Zhu, M.; Kang, N.; Sun, D. M.; Cheng, H. M.; Ren, W. Ultrafast Growth of Nanocrystalline Graphene Films by Quenching and Grain Size Dependent Strength and Bandgap Opening. *Nat. Commun.* **2019**, *10*, 4854.
(49) Ma, T.; Liu, Z.; Wen, J.; Gao, Y.; Ren, X.; Chen, H.; Jin, C.; Ma, X. L.; Xu, N.; Cheng, H. M.; Ren, W. Tailoring the Thermal and Electrical Transport Properties of Graphene Films by Grain Size Engineering. *Nat. Commun.* **2017**, *8*, 14486.